Inorganic Chemistry

Article

pubs.acs.org/IC

Cu Insertion Into the Mo_{12} Cluster Compound $Cs_2Mo_{12}Se_{14}$: Synthesis, Crystal and Electronic Structures, and Physical Properties

Rabih Al Rahal Al Orabi,[†] Bruno Fontaine,[†] Regis Gautier,[†] Patrick Gougeon,*[,†] Philippe Gall,[†] Yohan Bouyrie,[‡] Anne Dauscher,[‡] Christophe Candolfi,[‡] and Bertrand Lenoir[‡]

[†]Institut des Sciences Chimiques de Rennes, UMR 6226 CNRS−Université de Rennes 1−Ecole Nationale Supérieure de Chimie de Rennes, 11 allée de Beaulieu, CS 50837, 35708 Rennes Cedex, France

[‡]Institut Jean Lamour, UMR 7198 CNRS−Université de Lorraine, Parc de Saurupt, CS 50840, 54011 Nancy, France

Supporting Information

ABSTRACT: Mo-based cluster compounds are promising materials for high-temperature thermoelectric applications due to their intrinsic, extremely low thermal conductivity values. In this study, polycrystalline cluster compounds $Cs_2Cu_xMo_{12}Se_{14}$ were prepared for a wide range of Cu contents ($0 \le x \le 2$). All samples crystallize isostructurally in the trigonal space group $R\bar{3}$. The position of the Cu atoms in the unit cell was determined by X-ray diffraction on a single-crystalline specimen indicating that these atoms fill the empty space between the Mo−Se clusters. Density functional theory calculations predict a metallic ground state for all compositions, in good agreement with the experimental findings. Magnetization measurements indicate a rapid suppression of the superconducting state that develops in the $x = 0.0$ sample upon Cu insertion. Transport properties measurements, performed in a wide temperature range (2−630 K) on the two end-member compounds $x = 0$ and $x = 2$, revealed a multiband electrical conduction as shown by sign reversal of the thermopower as a function of temperature.

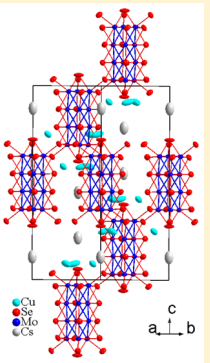

INTRODUCTION

The efficiency of thermoelectric materials is measured through the dimensionless figure of merit defined as $ZT = \alpha^2\sigma T/(\kappa_e + \kappa_L)$, where α is the Seebeck coefficient or thermopower, σ is the electrical conductivity, T is the absolute temperature, and κ_e and κ_L are the electronic and lattice thermal conductivities, respectively.[1,2] The higher the ZT, the more efficient the conversion of a temperature gradient into electricity (and vice versa). Because of the Wiedemann−Franz law that relates σ to κ_e, the optimization of the thermal transport without altering the electrical properties is extremely challenging. Thus, the minimization of the lattice thermal conductivity is one possible strategy to enhance the efficiency of thermoelectric materials. This can be achieved via several approaches such as nanostructuring, solid-solution alloying, or by searching for crystal structures exhibiting oversized cages that host heavy atoms according to the PGEC concept proposed by Slack.[3]

Compounds with a large and complex unit cell also offer a route toward extremely low thermal conductivity values. Their structural complexity is expected to shorten the phonon mean path, thereby efficiently disrupting the heat-carrying phonons. In this context, molybdenum cluster chalcogenides are of special interest due to their specific crystal structure based on molybdenum cluster units of general formula $Mo_{3n}Se^i_{3n+2}Se^a_6$ (where i and a stand for innen and außen, respectively, according to Schäfer's notation[4]). Besides the long-known Chevrel phases, several families of such cluster compounds have been investigated over the last years revealing interesting thermoelectric properties at high temperatures.

In $Ag_xMo_9Se_{11}$ ($3.4 \le x \le 3.9$),[5−7] each $Mo_9Se^i_{11}Se^a_6$ bioctahedral cluster is connected to four Mo_9 units via Mo−$Se^{i\text{-}a}$ bonds in such a way that large voids exist between clusters. The resulting cagelike crystal structure can accommodate silver cations that are delocalized over four different crystallographic sites. Investigations of the transport properties of $Ag_xMo_9Se_{11}$ ($3.4 \le x \le 3.9$) at low and high temperatures revealed a direct correlation between the Ag content and their thermoelectric performance.[6,7] Increasing x concomitantly lowers the thermal conductivity and increases the power factor. An interesting ZT of 0.65 at 800 K was measured for $Ag_{3.9}Mo_9Se_{11}$.[6] A comparable ZT value has been recently achieved in $Ag_2Tl_2Mo_9Se_{11}$, where bi-octahedral Mo_9 units are connected to six neighboring cluster units with Ag and Tl atoms partially occupying several crystallographic sites.[8]

The next level of complexity is provided by the $A_2Mo_{15}Se_{19}$ (A = In, Tl, alkali, or alkaline-earth atoms) family of compounds that crystallize in the trigonal space group $R\bar{3}$. The crystal structure is composed of a mixture of octahedral $Mo_6Se^i_8Se^a_6$ and bi-octahedral $Mo_9Se^i_{11}Se^a_6$ clusters in a 1:1 ratio connected through Mo−Se bonds;[9] the octahedral unit being similar to the one encountered in the Chevrel phases.[10] Because of the occurrence of large voids in its crystal structure, it was shown that three silver cations per formula unit could be inserted in the structure of $In_2Mo_{15}Se_{19}$, giving rise to $Ag_3In_2Mo_{15}Se_{19}$.[11] Such an insertion is possible owing to the

Received: March 31, 2016

DOI: 10.1021/acs.inorgchem.6b00781
Inorg. Chem. XXXX, XXX, XXX−XXX

overall nonbonding character of the top of the conduction band of $In_2Mo_{15}Se_{19}$. Although the thermal conductivity is comparable to that observed in $Ag_xMo_9Se_{11}$, $Ag_3In_2Mo_{15}Se_{19}$ exhibits a slightly lower ZT of 0.45 at 1100 K owing to lower thermopower values.[11] First-principles calculations have predicted that the carrier concentration of this compound could be further manipulated by adding a maximum of three more electrons per formula unit,[9] providing an experimental pathway to further enhance the thermopower.

Larger chalcogenide clusters of general formula Mo_{3n} (n = 4, 5, 6, 7, 8, 10, and 12), which result from the condensation of octahedral Mo_6 units via triangular face, were synthesized in our group. Among them, the $A_2Mo_2Se_{14}$ (A = Rb, Cs) compounds are based on $Mo_{12}Se^{i}_{14}Se^{a}_{6}$ clusters with the Mo_{12} core resulting from the face sharing of three octahedral Mo_6 clusters (Figure 1).[12,13] The trioctahedral Mo_{12} cluster is surrounded by 14

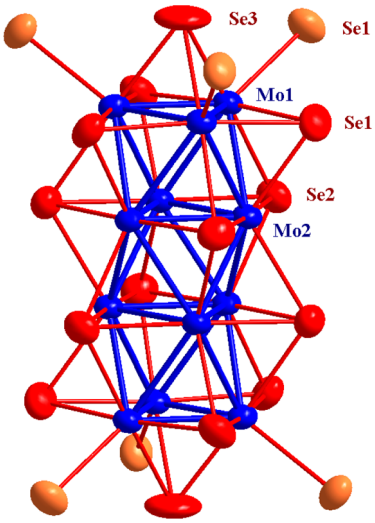

Figure 1. Perspective of the $Mo_{12}Se_{14}Se_6$ cluster unit.

"innen" Se atoms (in red in Figure 1) capping the triangular faces of the trioctahedron and 6 Se^a ligands (in orange in Figure 1) above the ending Mo atoms. Since it has been demonstrated that $[Mo_{12}Se_{14}]^{2-}$ could be further reduced without altering its structure, the possible insertion of several transition-metal cations such as copper was studied. Here, we report the syntheses, the crystal structure, the electronic density of states, and the magnetic properties of $Cu_xCs_2Mo_{12}Se_{14}$ for $0 \leq x \leq 2$. To evaluate the thermoelectric potential of these phases, transport and specific heat studies were made on the two end-member compounds x = 0 and x = 2 in a wide range of temperatures (2−800 K).

EXPERIMENTAL SECTION

Syntheses. Two precursors $MoSe_2$ and $Cs_2Mo_6Se_6$ together with elemental Cu and Mo were used in powder form as starting materials for the syntheses. The different manipulations of these reagents were performed in a purified Ar-filled glovebox to avoid contamination by oxygen and/or moisture. Elemental Mo powder was purified at 1273 K under H_2 flowing gas during 10 h to eliminate residual oxygen. $MoSe_2$ was prepared by direct reaction of Se and reduced Mo (ratio 2:1) in an evacuated (ca. 1×10^{-2} Pa residual pressure of Ar) and sealed quartz tube. The tube was then heated to 973 K and held at this temperature for 2 d.

The second precursor, $Cs_2Mo_6Se_6$, was prepared in two stages. First, $In_2Mo_6Se_6$ was obtained by mixing stoichiometric amounts of InSe, $MoSe_2$, and reduced Mo heated at 1273 K in an evacuated and sealed quartz tube during 36 h. Second, an ion-exchange reaction of $In_2Mo_6Se_6$ with CsCl was performed at 1073 K. For this purpose, $In_2Mo_6Se_6$ and CsCl powders were mixed in an approximate proportion of 1:2.5 and subsequently cold pressed. The cylindrical pellet was sealed under vacuum in a long quartz tube. One end of the tube containing the pellet was inside the furnace, while the other end (∼5 cm) was kept out of the furnace. The tube was maintained at 1073 K for 48 h. This reaction yielded white InCl crystals that grew at the cool end of the tube. Powder X-ray diffraction (PXRD) patterns, collected systematically after reaction, did not indicate the presence of any secondary phases. Pure polycrystalline samples of $Cs_2Mo_{12}Se_{14}$ were prepared by mixing $Cs_2Mo_6Se_6$, Mo, and $MoSe_2$ in stoichiometric quantities. The mixture was sealed in a molybdenum crucible under reduced argon pressure with an arc-welding apparatus and heated at 1573 K for 40 h. Polycrystalline samples of the quaternary compounds $Cs_2Cu_xMo_{12}Se_{14}$ (x = 0.5, 1.0, 1.5, and 2.0) were then synthesized by reacting Cu powder with $Cs_2Mo_{12}Se_{14}$ powder in evacuated silica tube at 1173 K for 48 h.

Single crystals of $Cs_2Mo_{12}Se_{14}$ were obtained by heating a powdered sample at 2023 K for 3 h, then cooled at a rate of 373 K h^{-1} to 1273 K, at which temperature the power was turned off. Single-crystalline specimens of $Cs_2Cu_xMo_{12}Se_{14}$ were synthesized by reacting Cu powder with $Cs_2Mo_{12}Se_{14}$ single crystals in evacuated silica tube at 1173 K for 48 h.

Densification. The different samples were ground into fine powders, which were subsequently consolidated into dense cylindrical-shaped pellets by spark plasma sintering using 10.4 mm inner diameter graphite die (SPS, Dr. Sinter 505 Syntex). The SPS processes were realized at 1523 and 1123 K for the x = 0.0 and 2.0 samples, respectively, for 10 min under 80 MPa. To prevent stickiness of plunger and sample, graphite foils were used. The geometric densities of the x = 0.0 and 2.0 samples, determined by dimensions and weight of the pellets, were 90% and 94%, respectively, of their theoretical values from crystallographic data.

Laboratory Powder X-ray Diffraction. Powder X-ray diffraction (PXRD) patterns were collected at 300 K on a D8 Bruker Advance diffractometer equipped with a LynxEye detector (Cu Kα_1 radiation, λ = 1.540 56 Å).

Scanning Electron Microscopy. Scanning electron microcopy (SEM) experiments were performed on bulk pieces of the x = 0.0 and 2.0 samples using a Quanta FEG 650 (FEI). Backscattered electron (BSE) images were taken to assess phase purity. Further elemental X-ray mappings were realized on selected areas to determine the distribution of the elements in the samples.

Differential Scanning Calorimetry. DSC measurements were conducted on powdered x = 0.0 and 2.0 samples in the temperature range of 300−650 K using a DSC121 apparatus (Setaram). Because of the low thermal conductivity of the present sample, we used a low heating rate (2 K min^{-1}) to obtain a good thermal equilibrium between the sample and the crucible.

Single-Crystal Structure Determination of $Cu_{1.3}Cs_2Mo_{12}Se_{14}$. Upon Cu insertion, most of the crystals tested on a Nonius Kappa CCD diffractometer (Mo Kα radiation, λ = 0.710 73 Å) were of poor quality and presented a substantial mosaic spread with values of ∼2 as calculated by DENZO.[14] For the investigated crystal, the mosaicity was of the order of 0.5, as usually found with good single crystals. The good quality of the specimen was further evidenced by the fact that all the Bragg spots found using the phi/chi procedure[15] could be indexed, indicating very minor twinning. The angular scan conditions (φ and ω scans) used over the data collection was calculated with the COLLECT program.[16] An absorption correction (T_{min} = 0.1570, T_{max} = 0.3141) based on the description of the crystal faces was used. The crystal structure was solved using the software Sir97[17] in space group $R\bar{3}$. Refinements and difference Fourier analyses were made with the SHELX software.[18] Refinement of the site occupancy factor for the Cu atoms yield the stoichiometry $Cu_{1.3}Cs_2Mo_{12}Se_{14}$ for the crystal investigated. Single-crystal data collection and structure refinement parameters for the $Cu_{1.3}Cs_2Mo_{12}Se_{14}$ compound are gathered in Table 1, while the atomic coordinates are given in Table

DOI: 10.1021/acs.inorgchem.6b00781
Inorg. Chem. XXXX, XXX, XXX−XXX

Table 1. Single-Crystal Data Collection and Structure Refinement Results for $Cu_{1.3}Cs_2Mo_{12}Se_{14}$

empirical formula	$Cu_{1.3}Cs_2Mo_{12}Se_{14}$
formula weight	2605.35
temperature	293(2) K
wavelength	0.710 69 A
crystal system, space group	trigonal, $R\bar{3}$
unit cell dimensions	a = 9.8952(4) Å, b = 9.8952(4) Å, c = 24.4248(10) Å
volume	2071.15(15) $Å^{-3}$
Z, calculated density	3, 6.267 Mg/m^{-3}
absorption coefficient	27.268 mm^{-1}
$F(000)$	3383
crystal size	0.10 × 0.08 × 0.05 mm
θ range for data collection	2.90° to 32.02°
limiting indices	$-12 \le h \le 14$, $-14 \le k \le 14$, $-33 \le l \le 36$
reflections collected/ unique	10 893/1608 [R(int) = 0.0296]
completeness to θ = 32.02	99.9%
refinement method	full-matrix least-squares on F^2
data/restraints/ parameters	1608/0/55
goodness-of-fit on F^2	1.120
final R indices [$I > 2\sigma(I)$]	$R1$ = 0.0298, $wR2$ = 0.0578
R indices (all data)	$R1$ = 0.0408, $wR2$ = 0.0613
extinction coefficient	0.000 085(12)
largest diff peak and hole	3.090 and −2.000 e·$Å^{-3}$

2, and selected interatomic distances are in Table 3. Additional crystallographic information is available in the Supporting Information.

Magnetometry. Magnetic susceptibility measurements were performed using a Quantum Design MPMS-XL SQUID magnetometer. Measurements were made in direct-current fields of 10 Oe between 1.8 and 7 K on powdered samples.

Transport Properties Measurements. For transport properties measurements, disc- and bar-shaped samples (⌀12 mm and 2 × 2 × 8 mm^3, respectively) were cut in the consolidated pellets with a diamond wire saw. Electrical resistivity, thermopower, and thermal conductivity were measured at the same time in the 5−350 K temperature range using the thermal transport option of a physical property measurement system (PPMS, Quantum Design). Good electrical and thermal contacts on the samples were ensured by attaching four copper leads glued with a small amount of conducting silver epoxy. The samples with the attached leads were then heated to 403 K for 10 min to harden the epoxy and get mechanically stable contacts. The Hall coefficient R_H was measured using a five-probe method with the alternating current transport option of the PPMS in the same temperature range. Five copper wires were attached on the samples with a tiny amount of silver paste. The carrier density p was calculated from R_H based on $p = r_H/R_H e$, where e is the elementary charge, assuming a scattering factor r_H of 1 within a single-carrier picture. Specific heat C_p data were collected using the dedicated option of the PPMS in the 2−300 K temperature range. For this measurement, a small dense sample of ∼20 mg was glued on the platform of the sample holder using a minute amount of Apiezon N grease.

High-temperature electrical resistivity and thermopower were simultaneously measured with a ZEM-3 setup (Ulvac-Riko) between 300 and 623 K. Thermal diffusivity a was measured in the 300−623 K temperature range using a laser flash technique (LFA 467, Netzsch). Thermal conductivity was then calculated via $\kappa = aC_p d$, where d is the geometric density. In the present case, the temperature dependence of d was neglected. The C_p values were considered temperature-independent above 300 K and equal to the Dulong−Petit value of $3NR$ in which N is the number of atoms per formula unit and R is the gas constant.

Computational Details. Density functional band structure calculations were realized on $Cs_2Mo_{12}Se_{14}$ with the scalar relativistic tight-binding linear muffin-tin orbital (LMTO) method in the atomic spheres approximation including combined correction.[19] The exchange-correlation interaction was treated within the local density approximation using the von Barth−Hedin local potential.[20] The optimal positions and radii (r_{ES}) of interstitial spheres (also called empty spheres (ES)), used to fill interatomic spaces, were obtained by the automatic procedure reported in ref 19g. Seven nonsymmetry-related ES with 0.72 Å ≤ r_{ES} ≤ 1.30 Å were introduced in these calculations. We used a full LMTO basis set composed of 6s, 6p, 5d, and 4f functions for Cs spheres, 5s, 5p, 4d, and 4f functions for Mo spheres, 4s, 4p, and 4d for Se spheres, and s, p, and d functions for ES. Following the Löwdin downfolding technique, the Cs 6s, 6p; Mo 5s, 5p, 4d; Se 4s, 4p; and interstitial 1s LMTOs were used as the minimal basis set to solve the eigenvalue problem. To this end, k-space integration was performed using the tetrahedron method.[21] Charge self-consistency and averaged properties were obtained from 40 irreducible k points. The crystal orbital Hamiltonian populations (COHP) corresponding to the Hamiltonian population weighted density of states (DOS) was computed to gain insights into the magnitude of the bonding.[22] As advised, we used a reduced basis set (in which all ES LMTOs are downfolded) for the COHP calculations.

Table 3. Main Interatomic Distances (Å) in $Cu_{1.3}Cs_2Mo_{12}Se_{14}$

Mo(1)−Mo(1)	2.6241(8)	Cu(1)−Se(3)	2.077(4)
Mo(1)−Mo(2)	2.7253(6)	Cu(1)−Se(1)	2.220(4)
Mo(1)−Mo(2)	2.7542(6)	Cu(1)−Se(2)	2.350(4)
Mo(1)−Se(3)	2.5586(9)		
Mo(1)−Se(1)	2.6022(7)	Cs(1)−Se(2) (×3)	3.6502(6)
Mo(1)−Se(1)	2.6459(7)	Cs(1)−Se(1) (×3)	3.7845(8)
Mo(1)−Se(2)	2.6879(7)	Cs(1)−Se(3)	3.9184(14)
Mo(1)−Se(1)	2.6900(7)	Cs(1)−Se(2) (×3)	4.0238(8)
Mo(2)−Mo(2)	2.6885(8)		
Mo(2)−Mo(2)	2.6945(7)		
Mo(2)−Se(2)	2.6078(7)		
Mo(2)−Se(2)	2.6092(7)		
Mo(2)−Se(1)	2.6170(7)		
Mo(2)−Se(2)	2.6734(6)		

Table 2. Fractional Atomic Coordinates and Equivalent Isotropic Displacement Parameters ($Å^2$) for the Compound $Cu_{1.3}Cs_2Mo_{12}Se_{14}$

atom	Wyckoff position	x	y	z	Ueq	s.o.f
Cu1	18f	0.7201(6)	0.1666(5)	0.583 78(15)	0.0293(13)	0.217(4)
Cs1	6c	1.3333	0.6667	0.783 80(4)	0.0376(3)	1
Mo1	18f	0.810 52(5)	0.494 26(5)	0.695 305(16)	0.009 35(10)	1
Mo2	18f	0.830 06(5)	0.347 33(5)	0.788 243(16)	0.008 67(10)	1
Se1	18f	0.990 32(6)	0.372 54(6)	0.699 79(2)	0.013 33(12)	1
Se2	18f	0.956 58(6)	0.650 25(6)	0.786 71(2)	0.013 05(12)	1
Se3	6c	0.6667	0.3333	0.610 89(4)	0.0260(2)	1

DOI: 10.1021/acs.inorgchem.6b00781
Inorg. Chem. XXXX, XXX, XXX−XXX

RESULTS AND DISCUSSION

Electronic Structure. Chalcogenide cluster compounds containing polynuclear transition metals have focused attention because of their unique structural properties. Regardless of the nature of the transition metal, electron counts of octahedral-based M_{3n} clusters ($n > 3$) are not explained within the existing electron-counting rules.[23] For instance, $Ni_{12}Se_{12}(P(CH_2CH_3)_3)_6$ has 96 metallic electrons (ME), that is, electrons available for metal−metal bonds. According to a qualitative analysis supported by density functional theory (DFT) calculations, only two strongly metal−metal bonding molecular orbitals are occupied for this ME count.[24] The ME count of Mo_{12} cluster in $Cs_2Mo_{12}Se_{14}$ is lower than that of the nickel analogue: assuming an oxidation state of +I for the alkaline metal, the ME count for the $[Mo_{12}Se_{14}]^{2-}$ motif is equal to 46. Using extended Hückel calculations, Hughbanks and Hoffmann showed that an ME count of 50 could be reached for such a unit owing to the nodal properties of the lowest vacant molecular orbitals of the $Mo_{12}Se_{14}$ unit.[25] This prediction was later confirmed for such an isolated unit using DFT calculations on $[Mo_{12}Se_{14}]^{n-}$ (n = 2, 6).[26] The calculated total and Mo-projected density of states (DOS) are sketched in Figure 2. The

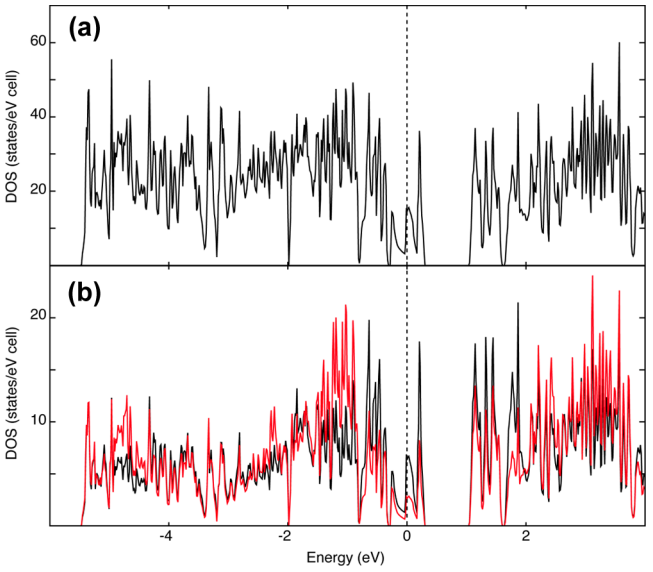

Figure 2. DFT DOS of $Cs_2Mo_{12}Se_{14}$: (a) total, (b) Mo1 (black) and Mo2 (red) projections. DOS are shifted so that the Fermi level lies at 0 eV.

top of the valence band is mainly centered on Mo atoms; slightly more on Mo1 than Mo2. This is consistent with the DFT calculations performed on an isolated $Mo_{12}Se_{14}$ unit.[26] The gap between the valence and the conduction bands is ~0.7 eV. According to the DOS, a metallic behavior is expected for this compound in agreement with prior electrical conductivity measurements performed on a single-crystalline specimen.[13]

COHP curves computed for several Mo−Mo contacts are presented in Figure 3. These curves show that both Mo1−Mo1 (2.656 Å) and Mo2−Mo2 bonds (2.682 Å) are optimized in $Cs_2Mo_{12}Se_{14}$. Assuming a rigid-band approach, reducing this compound should weaken these bonds because of the antibonding character of the bands at the top of the valence band. In contrast, such a reduction should strengthen the Mo1−Mo2 bonds, since the bands that lie at the top of the valence band show a Mo1−Mo2 bonding character. As

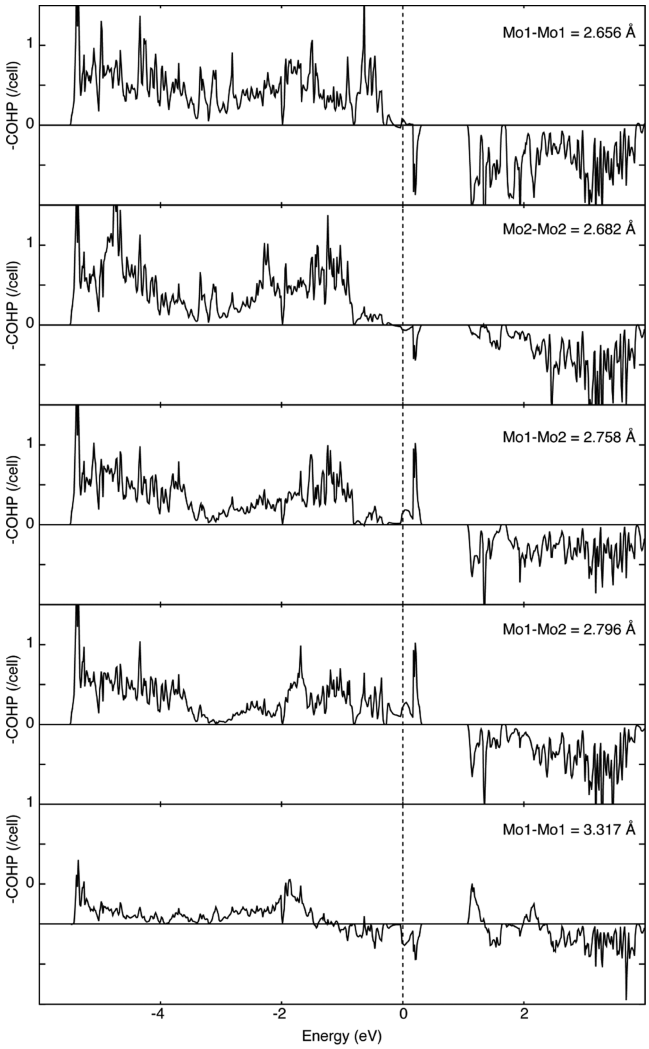

Figure 3. DFT COHP computed for several Mo−Mo bonds of $Cs_2Mo_{12}Se_{14}$. COHP are shifted so that the Fermi level lies at 0 eV.

expected for intercluster Mo−Mo bonds, the absolute COHP values of valence and conduction bands are smaller than that of metal−metal bonds within the Mo_{12} cluster. However, the integrated COHP of intercluster Mo−Mo bond is about the quarter of that of the Mo−Mo bonds in the Mo_{12} cluster. The COHP averaged over all Mo−Mo bonds within the cluster (not shown here) show that the top of the valence band has an overall nonbonding character. Hence, provided a rigid-band model is valid, reduction of $Cs_2Mo_{12}Se_{14}$ should be possible with a maximum of four electrons without altering its architecture.

Phase Purity and Chemical Homogeneity. As shown in Figure 4, single-phase samples were obtained up to a Cu content of x = 2.0. Beyond this limit, increasing amounts of the Chevrel phase $Cu_xMo_6Se_8$ as the main impurity could be observed. The variations in the lattice parameters a and c, obtained from the analyses of the PXRD patterns by the Le Bail method,[27] along with the unit cell volume as a function of the Cu content, are shown in Figure 5a,b. Inserting Cu into $Cs_2Mo_{12}Se_{14}$ leads to an increase in a, while c tends to decrease (Figure 5a). These variations show that the a parameter is mainly governed by the sterical effect due to Cu insertion, while the decrease in c is controlled by an electronic effect that leads to a contraction of the Mo_{12} cluster (see above). Despite these

DOI: 10.1021/acs.inorgchem.6b00781
Inorg. Chem. XXXX, XXX, XXX−XXX

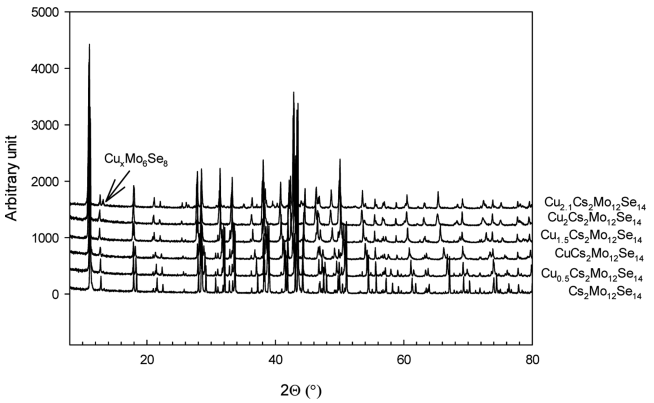

Figure 4. PXRD patterns of $Cs_2Mo_{12}Se_{14}$, $Cu_{0.5}Cs_2Mo_{12}Se_{14}$, $CuCs_2Mo_{12}Se_{14}$, $Cu_{1.5}Cs_2Mo_{12}Se_{12}$, $Cu_2Cs_2Mo_{12}Se_{14}$, and $Cu_{2.1}Cs_2Mo_{12}Se_{14}$.

opposite trends, the unit cell volume increases quasi-linearly with the Cu content (Figure 5b).

The SEM images collected in BSE mode and the corresponding elemental X-ray mapping (Figures S1 and S2) revealed a homogeneous distribution of the elements in $Cs_2Mo_{12}Se_{14}$. No noticeable impurity phases could be observed except for small amounts of CsCl used as a starting agent for ionic exchange. For $Cu_2Cs_2Mo_{12}Se_{14}$, these analyses indicate an overall good chemical homogeneity of the Cs, Mo, and Se elements. However, Cu tends to be less well-distributed within the matrix resulting in slight variations in the Cu content in the sample's volume.

Crystal Structure. A view of the structure of $Cu_xCs_2Mo_{12}Se_{14}$ is represented in Figure 6. The Mo−Se framework corresponds to that of $Cs_2Mo_{12}Se_{14}$ and is based on $Mo_{12}Se_{14}Se_6$ cluster units linked through Mo−Se interunit bonds (Figure 1). The $Mo_{12}Se_{14}Se_6$ is centered at the *6b* position and has the point-group symmetry −3. The variation of the cationic charge transfers toward the Mo_{12} clusters in $Cs_2Mo_{12}Se_{14}$ and $Cu_{1.3}Cs_2Mo_{12}Se_{14}$, that is, +2 and +3.3, respectively, induces some variations in the Mo−Mo distances. Thus, the Mo−Mo bond lengths in the Mo_{12} clusters in $Cu_{1.3}Cs_2Mo_{12}Se_{14}$ are 2.6241(8) and 2.6885(8) Å in the triangles formed by the Mo1 and Mo2 atoms, respectively, while in $Cs_2Mo_{12}Se_{14}$, they are equal to 2.656(1) and 2.682(1) Å, respectively. The Mo−Mo bond lengths between the triangles formed by the Mo1 and Mo2 atoms are 2.7253(6) and 2.7542(6) Å in $Cu_{1.3}Cs_2Mo_{12}Se_{14}$ compared to 2.758(1) and 2.796(1) Å in $Cs_2Mo_{12}Se_{14}$. The Mo2−Mo2 distances

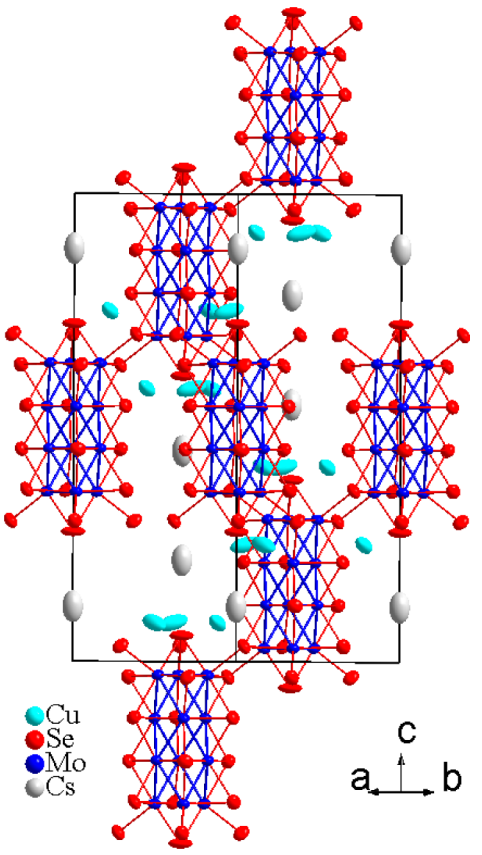

Figure 6. View of the crystal structure of $Cu_{1.3}Cs_2Mo_{12}Se_{14}$ along the [110] direction.

between the two internal triangles are equal to 2.6945(7) Å instead of 2.682(1) Å in $Cs_2Mo_{12}Se_{14}$. All these variations are consistent with the various Mo−Mo COHP curves computed for $Cs_2Mo_{12}Se_{14}$ (see Figure 3). Consequently, the Cu insertion led to a contraction of the Mo_{12} cluster with a distance between the two ending Mo_3 triangles of 6.74 Å in $Cu_{1.3}Cs_2Mo_{12}Se_{14}$ compared to 6.81 Å in $Cs_2Mo_{12}Se_{14}$. The Mo−Se bond lengths are almost unchanged by the cationic charge and are comprised between 2.5586(9) and 2.6900(7) Å. The three-dimensional arrangement arises from the interconnection of the $Mo_{12}Se_{14}Se_6$ units through Mo1−Se1 bonds. Indeed, each unit is linked to six adjacent units via 6 Mo1−Se1 bonds and six Se1−Mo1 bonds. As a consequence, the shortest Mo1−Mo1 distance between adjacent Mo_{12} clusters is 3.502(1) Å

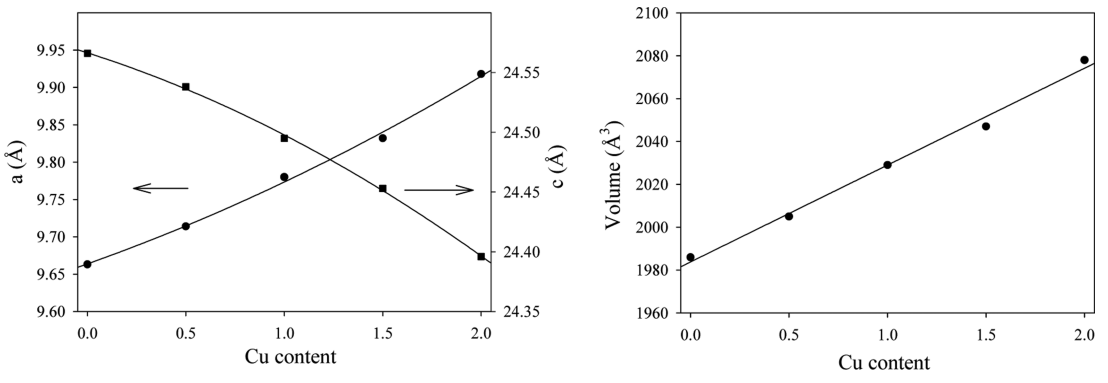

Figure 5. Unit cell parameters (*a*, *c*, and volume) of $Cu_xCs_2Mo_{12}Se_{14}$ (x = 0.0, 0.5, 1.0, 1.5, and 2.0).

DOI: 10.1021/acs.inorgchem.6b00781
Inorg. Chem. XXXX, XXX, XXX−XXX

(3.317(1) Å in $Cs_2Mo_{12}Se_{14}$) that reflects very weak Mo−Mo interaction.

The Cu atoms reside in triangular sites located around the threefold axes near the Cs sites with Cu−Se distances of 2.077(4), 2.220(4), and 2.350(4) Å (Figure 7). On the one

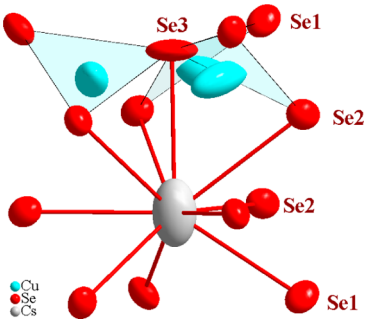

Figure 7. Selenium environments around the Cs and Cu atoms.

hand, it should be kept in mind that the latter distances are only indicative, since they are comprised between values observed in the empty and full sites due to the Cu deficiency. On the other hand, the strongly anisotropic displacement parameters of the copper is a tendency often found in other sulfur or selenium compounds.[28−30] The Cu insertion yields a change in the Cs environment with an increase in the Cs−Se3 and Cs−Se2 distances. Indeed, the latter two distances are equal to 3.9184(14) and 4.0238(8) Å in $Cu_{1.3}Cs_2Mo_{12}Se_{14}$, while they equal to 3.769(1) and 3.791(1) Å in $Cs_2Mo_{12}Se_{14}$. The other Se atoms are at 3.6502(6) Å (3 Se2 atoms) and 3.7845(8) Å (3 Se1 atoms).

Superconductivity in $Cs_2Cu_xMo_{12}Se_{14}$ ($0 \le x \le 2$). The superconducting properties of $Cs_2Mo_{12}Se_{14}$ have been the subject of a prior detailed study performed on a single-crystalline specimen.[31] Hence, we restrict our investigation herein to the evolution of the superconducting transition temperature upon inserting Cu. Evidence that bulk superconductivity develops in $Cs_2Mo_{12}Se_{14}$ is provided by the specific heat data shown in Figure 8. A clear λ-type jump in C_p

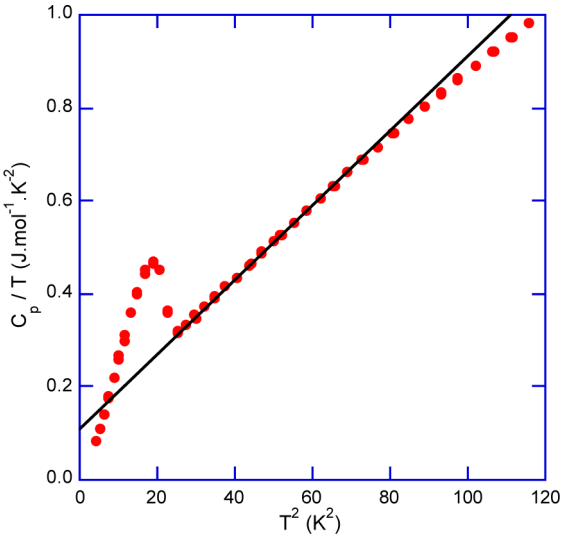

Figure 8. Specific heat data of the $x = 0.0$ sample plotted as C_p/T vs T^2. The jump at ~4.4 K corresponds to the superconducting transition. The solid black line is a guide.

at ~4.5 K corresponds to the superconducting transition. In the normal state, the data between 5 and 8 K were fitted to the free-electron relation $C_p = \gamma T + \beta T^3$, where γT and βT^3 are the electronic and the phonon contributions, respectively. The best fit to the data yields $\gamma \approx 120$ mJ mol^{-1} K^{-2} and a Debye temperature θ_D of ~190 K derived from β, both of which being in excellent agreement with those inferred on single-crystals. Such high γ-value is consistent with a large DOS at the Fermi level predicted by our first-principles calculations. The electronic specific heat (Figure S3 in Supporting Information) was obtained by subtracting the phonon contribution leading to a specific heat jump ΔC of roughly 1.5 γT_c. This value is close to the simple *s*-wave BCS prediction (1.43 γT_c) but lower than that measured on single-crystals (~2.15 γT_c), the difference being likely due to the polycrystalline nature of the present sample.

Zero-field cooled magnetization data, shown in Figure 9, are consistent with the specific heat data and show that the

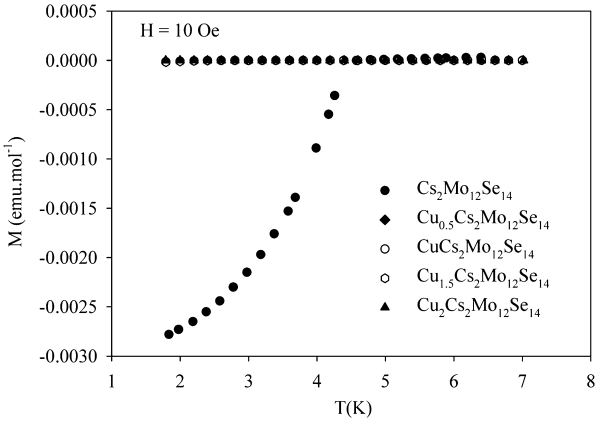

Figure 9. Temperature dependence of the magnetic susceptibility of polycrystalline samples of $Cu_xCs_2Mo_{12}Se_{14}$ (x = 0.0, 0.5, 1.0, 1.5, and 2.0).

superconducting transition appears sharply at 4.4 K in the x = 0.0 sample. Superconductivity is, however, rapidly suppressed upon Cu insertion since none of the Cu-containing samples show signs of a transition down to 1.8 K, suggesting a drastic decrease in the electron−phonon coupling strength with x.

Transport Properties. For both samples, the thermopower shows a complex, nonlinear behavior with increasing temperature (Figure 10). The relatively low values measured are consistent with the metallic ground state predicted by our electronic band structure calculations. In $Cs_2Mo_{12}Se_{14}$, the negative values observed at low temperatures reach a minimum near 50 K before decreasing (in absolute values) steadily and eventually becoming positive above 550 K. Upon Cu insertion, this behavior remains qualitatively similar, although the whole $\alpha(T)$ curve is shifted up by ~20 μV K^{-1} leading to a crossover from negative to positive values at 150 K. Above room temperature, the α values monotonically increase to reach 40 μV K^{-1} at 600 K. Both the nonlinear behavior and the sign change indicate that n- and p-type charge carriers contribute to the electrical conduction. Although experimental evidence that other Mo-based cluster compounds also harbor a mixed electrical conduction have been reported,[7,8,11] none of the compounds investigated so far had shown negative α values either at low or at high temperatures.

DOI: 10.1021/acs.inorgchem.6b00781
Inorg. Chem. XXXX, XXX, XXX−XXX

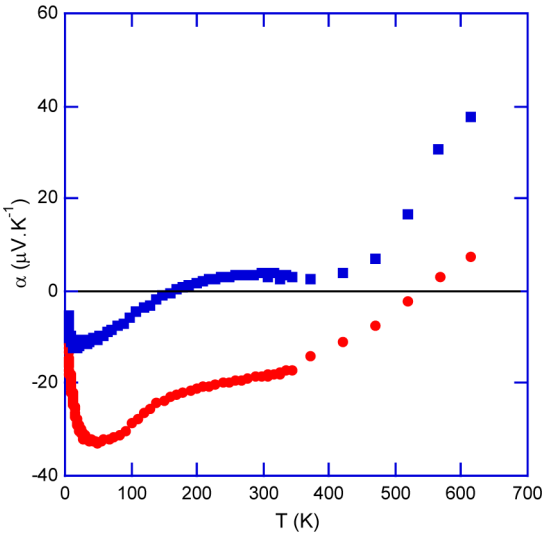

Figure 10. Thermopower of the x = 0.0 (red ●) and 2.0 (blue ■) samples as a function of temperature. The solid horizontal black line is drawn to indicate the temperature at which the sign of α reverses.

The Hall resistivity ρ_H measured in the x = 2.0 sample retains a positive and linear behavior as a function of the magnetic field $\mu_0 H$ in the whole temperature range (not shown). The difference in the sign of thermopower and Hall coefficient is another evidence of the bipolar nature of the electrical conduction in these materials. The dominant, positive hole-like signal further suggests that holes likely occupy bands with low density-of-states effective mass giving rise to high mobilities. In contrast, the negative thermopower values below 150 K may originate from electrons residing in high-mass bands leading to a positive partial thermopower that outweighs that of holes.

The Hall carrier density p_H, shown in Figure 11 as a function of the temperature, has no significant change from 300 K to ~150 K (~9 × 10^{20} cm^{-3}) and then starts decreasing upon further cooling to reach 4.4 × 10^{20} cm^{-3} at 15 K. The temperature at which the change in behavior occurs coincides

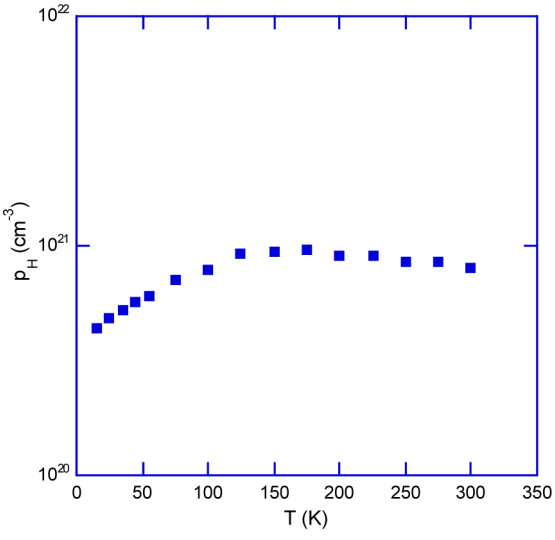

Figure 11. Temperature dependence of the Hall carrier concentration p_H of the x = 2.0 sample derived from the Hall coefficient within a single-carrier picture.

with the n-to-p-type transition seen in $\alpha(T)$. This abnormal change in carrier concentration is a consequence of the opposing role of holes and electrons leading to compensation effects in the Hall coefficient. Of note, because these materials are two-carrier systems, the Hall carrier concentrations given herein are only upper limits of the actual hole and electron concentrations and should therefore be taken with some caution.

Figure 12 shows the temperature dependence of the electrical resistivity. For $Cs_2Mo_{12}Se_{14}$, ρ exhibits a metallic

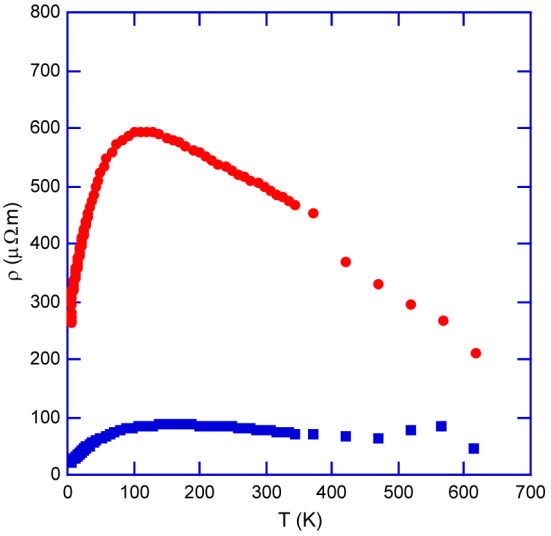

Figure 12. Electrical resistivity of the x = 0.0 (red ●) and 2.0 (blue ■) samples as a function of temperature.

behavior below ~100 K, the temperature at which a maximum is reached. Above this temperature, ρ significantly decreases upon heating to 600 K. The strong variations in ρ with temperature, the change in behavior around 100 K, and the large values measured are all consistent with the semimetallic nature of the transport in this material and with prior measurements performed on single crystals along the c axis.[13,26] The $\rho(T)$ data of $Cs_2Cu_2Mo_{12}Se_{14}$ show a similar behavior, although the presence of Cu strongly lowers the values and their variations in temperature. Furthermore, this specimen presents an anomaly around 550 K that corresponds to a thermal event detected in the DSC trace (Figure S4) and to a hump seen in the $\kappa(T)$ curve (see below). It is worth mentioning that this hump was observed in several runs performed with distinct samples and thus is intrinsic to the sample studied. Although the origin of this anomaly remains unknown, this might hint at diffusion of Cu atoms in the crystal structure.

The total thermal conductivity κ of the two end-member compounds is shown in Figure 13. The electronic contribution κ_e was estimated from the Wiedemann–Franz law $\kappa_e = LT/\rho$, where L is the Lorenz number. As a first approximation, we assumed that L is equal to the degenerate limit; that is, L_0 = 2.45 × 10^{-8} V^2 K^{-2}. The lattice contribution $\kappa_L = \kappa - \kappa_e$ is low, ~0.75 W m^{-1} K^{-1} at 300 K in the x = 0.0 sample, and is comparable to that achieved in other Mo-based cluster compounds.[7,8,11] Interestingly, the introduction of Cu does not result in a further decrease in κ_L as it may be naively expected from enhanced alloy-disorder scattering. We note that the slight difference in the experimental density of the two

DOI: 10.1021/acs.inorgchem.6b00781
Inorg. Chem. XXXX, XXX, XXX–XXX

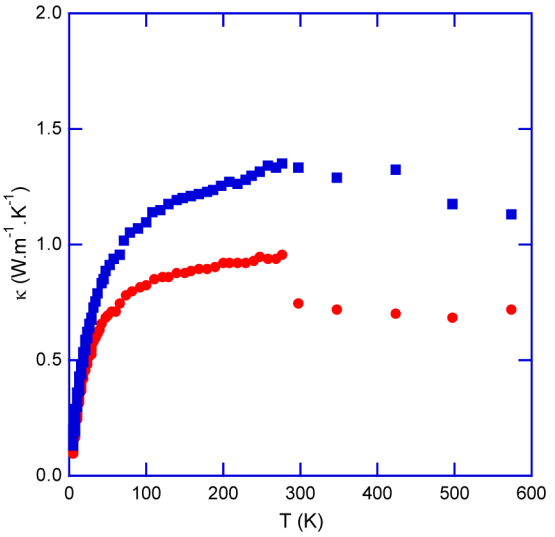

Figure 13. Temperature dependence of the total thermal conductivity of the x = 0.0 (red ●) and 2.0 (blue ■) samples. For x = 0.0, the discrepancy between the low- and high-temperature data sets at 300 K is due to the radiative contribution superimposed to the intrinsic κ values above 200 K.

specimens cannot account for the observed behavior. This trend is similar to that observed in the Mo_3Sb_7-based thermoelectric compounds where a significant increase in the lattice thermal conductivity occurs upon substituting Sb for Te or Ru for Mo.[32−36] In this system, the superconducting transition that sets in at 2.3 K in Mo_3Sb_7 is rapidly suppressed upon Te or Ru alloying.[37−43] Recent inelastic neutron and X-ray scattering measurements have shown that this strong suppression in electron−phonon coupling leads to a concomitant increase in the phonon group velocities, thereby lowering phonon scattering rates.[44] This mechanism outweighs the effect of point-defect scattering and thus results in an increase in the lattice thermal conductivity despite enhanced disorder in the unit cell. The fact that insertion of Cu in $Cs_2Mo_{12}Se_{14}$ also efficiently destroys superconductivity suggests that electron−phonon coupling has a strong influence on the thermal transport in $Cs_2Mo_{12}Se_{14}$.

CONCLUSION

The effects of Cu insertion in the crystal structure, electronic band structure, and transport properties of the Mo-based cluster compound $Cs_2Mo_{12}Se_{14}$ have been investigated. Polycrystalline phase-pure samples could be prepared up to x = 2.0 according to PXRD measurements. Although both compounds exhibit metallic behavior in agreement with first-principles calculations, the superconducting transition that sets in at 4.4 K in $Cs_2Mo_{12}Se_{14}$ is rapidly suppressed upon Cu insertion. This decrease in the electron−phonon coupling strength likely plays a role in the increase in the thermal conductivity observed in the Cu-containing sample with respect to the parent compound despite enhanced disorder in the unit cell. Thermopower features a complex temperature dependence evidencing a multiband nature of the electrical transport in both compounds. Because of the opposite and detrimental influence of both carriers on the thermopower, the ZT values remain very low, indicating that further adjustment of the carrier concentration is required. Optimization may be investigated through aliovalent insertion and/or substitutions to drive the system closer to a semiconducting state.

ASSOCIATED CONTENT

Supporting Information

The Supporting Information is available free of charge on the ACS Publications website at DOI: 10.1021/acs.inorgchem.6b00781. More details on the crystal structure study can be got from the Fachinformationszentrum Karlsruhe, 76344 Eggenstein-Leopoldshafen, Germany, (fax: (49) 7247−808−666; e-mail: crysdata@fiz.karlsruhe.de) on quoting the depository number CSD-428082.

BSE image of a fracture area and X-ray mapping for $Cs_2Mo_{12}Se_{14}$; BSE image and X-ray mapping for $Cs_2Cu_2Mo_{12}Se_{14}$; temperature dependence of the electronic specific heat C_{el} plotted as C_{el}/T versus T of $Cu_2Mo_{12}Se_{14}$ after subtraction of the lattice contribution; DSC trace upon heating for the x = 2.0 sample. (PDF)
Crystallographic data in CIF format. (CIF)

AUTHOR INFORMATION

Corresponding Author

*E-mail: patrick.gougeon@univ-rennes1.fr.

Notes

The authors declare no competing financial interest.

REFERENCES

(1) Goldsmid, H. J. In *Thermoelectric Refrigeration;* Temple Press Books Ltd: London, U.K., 1964.
(2) *Thermoelectrics and Its Energy Harvesting;* Rowe, D. M., Ed.; CRC Press: Boca Raton, FL, 2012.
(3) Slack, G. A. *CRC Handbook of Thermoelectrics;* Rowe, D. M., Ed.; CRC Press: Boca Raton, FL, 1995; p 407.
(4) Schäfer, H.; Schnering, H. G. *Angew. Chem.* **1964**, *76*, 833−849.
(5) Gougeon, P.; Padiou, J.; Lemarouille, J. Y.; Potel, M.; Sergent, M. *J. Solid State Chem.* **1984**, *51*, 218−226.
(6) Zhou, T.; Lenoir, B.; Colin, M.; Dauscher, A.; Al Orabi, R. A. R.; Gougeon, P.; Potel, M.; Guilmeau, E. *Appl. Phys. Lett.* **2011**, *98*, 162106.
(7) Zhou, T.; Colin, M.; Candolfi, C.; Boulanger, C.; Dauscher, A.; Santava, E.; Hejtmanek, J.; Baranek, P.; Al Rahal Al Orabi, R.; Potel, M.; Fontaine, B.; Gougeon, P.; Gautier, R.; Lenoir, B. *Chem. Mater.* **2014**, *26*, 4765−4775.
(8) Al Rahal Al Orabi, R.; Gougeon, P.; Gall, P.; Fontaine, B.; Gautier, R.; Colin, M.; Candolfi, C.; Dauscher, A.; Hejtmanek, J.; Malaman, B.; Lenoir, B. *Inorg. Chem.* **2014**, *53*, 11699−11709.
(9) Potel, M.; Chevrel, R.; Sergent, M. *Acta Crystallogr., Sect. B: Struct. Crystallogr. Cryst. Chem.* **1981**, *37*, 1007−1010.
(10) Chevrel, R.; Sergent, M.; Prigent, J. *J. Solid State Chem.* **1971**, *3*, 515−519.
(11) Gougeon, P.; Gall, P.; Al Rahal Al Orabi, R.; Fontaine, B.; Gautier, R.; Potel, M.; Zhou, T.; Lenoir, B.; Colin, M.; Candolfi, C.; Dauscher, A. *Chem. Mater.* **2012**, *24*, 2899−2908.
(12) Gougeon, P.; Potel, M.; Padiou, J.; Sergent, M. *Mater. Res. Bull.* **1987**, *22*, 1087.
(13) Gautier, R.; Picard, S.; Gougeon, P.; Potel, M. *Mater. Res. Bull.* **1999**, *34*, 93.
(14) Otwinowski, Z.; Minor, W. *Methods Enzymol.* **1997**, *276*, 307−326.
(15) Duisenberg, A. J. M. Ph.D. Thesis, University of Utrecht: Utrecht, The Netherlands, 1998.
(16) Nonius, B. V. COLLECT, data collection software; Nonius BV: Delft, The Netherlands, 1999.

DOI: 10.1021/acs.inorgchem.6b00781
Inorg. Chem. XXXX, XXX, XXX−XXX

(17) Altomare, A.; Burla, M. C.; Camalli, M.; Cascarano, G. L.; Giacovazzo, C.; Guagliardi, A.; Moliterni, A. G. G.; Polidori, G.; Spagna, R. *J. Appl. Crystallogr.* **1999**, *32*, 115−119.
(18) Sheldrick, G. M. *Acta Crystallogr., Sect. A: Found. Crystallogr.* **2008**, *64*, 112−122.
(19) (a) Andersen, O. K. *Phys. Rev. B* **1975**, *12*, 3060−3083. (b) Andersen, O. K. *Europhys. News* **1981**, *12*, 4−8. (c) Andersen, O. K. In *The Electronic Structure Of Complex Systems;* Phariseau, P., Temmerman, W. M., Eds.; Plenum Publishing Corporation: New York, 1984. (d) Andersen, O. K.; Jepsen, O. *Phys. Rev. Lett.* **1984**, *53*, 2571−2574. (e) Andersen, O. K.; Jepsen, O.; Sob, M. In *Electronic Band Structure and its Application;* Yussouf, M., Ed.; Springer-Verlag: Berlin, Germany, 1986. (f) Skriver, H. L. *The LMTO Method;* Springer-Verlag: Berlin, Germany, 1984. (g) Jepsen, O.; Andersen, O. K. *Z. Phys. B: Condens. Matter* **1995**, *97*, 35.
(20) von Barth, U.; Hedin, L. *J. Phys. C: Solid State Phys.* **1972**, *5*, 1629−1642.
(21) Blöchl, P. E.; Jepsen, O.; Andersen, O. K. *Phys. Rev. B: Condens. Matter Mater. Phys.* **1994**, *49*, 16223−16233.
(22) Dronskowski, R.; Blöchl, P. E. *J. Phys. Chem.* **1993**, *97*, 8617−8624.
(23) (a) Mingos, D. M. P.; Johnston, R. L. *Struct. Bonding (Berlin) 68*, 1987. (b) Mingos, D. M. P.; Wales, D. J. In *Introduction to Cluster Chemistry;* Prentice Hall: Englewood Cliffs, 1990.
(24) Gautier, R.; Furet, E.; Halet, J.-F.; Lin, Z.; Saillard, J.-Y.; Xu, Z. *Inorg. Chem.* **2002**, *41*, 796.
(25) Hughbanks, T.; Hoffmann, R. *J. Am. Chem. Soc.* **1983**, *105*, 1150.
(26) Gautier, R.; Gougeon, P.; Halet, J.-F.; Potel, M.; Saillard, J.-Y. *J. Alloys Compd.* **1997**, *262−263*, 311.
(27) Le Bail, A. *Powder Diffr.* **2005**, *20*, 316.
(28) Gaudin, E.; Petricek, V.; Boucher, F.; Taulelle, F.; Evain, M. *Acta Crystallogr., Sect. B: Struct. Sci.* **2000**, *B56*, 972−979.
(29) Berger, R.; Eriksson, L. J. *J. Less-Common Met.* **1990**, *161*, 101.
(30) McGuire, M.; Ranjan, C.; DiSalvo, F. *Inorg. Chem.* **2006**, *45*, 2718−2726.
(31) Brusetti, R.; Laborde, L.; Sulpice, A.; Calemczuk, R.; Potel, M.; Gougeon, P. *Phys. Rev. B: Condens. Matter Mater. Phys.* **1995**, *52*, 4481.
(32) Candolfi, C.; Lenoir, B.; Dauscher, A.; Guilmeau, E.; Hejtmanek, J.; Tobola, J.; Wiendlocha, B.; Kaprzyk, S. *Phys. Rev. B: Condens. Matter Mater. Phys.* **2009**, *79*, 035114.
(33) Candolfi, C.; Lenoir, B.; Dauscher, A.; Hejtmanek, J.; Tobola, J. *Phys. Rev. B: Condens. Matter Mater. Phys.* **2009**, *79*, 235108.
(34) Candolfi, C.; Lenoir, B.; Dauscher, A.; Hejtmanek, J.; Tobola, J. *Phys. Rev. B: Condens. Matter Mater. Phys.* **2009**, *80*, 155127.
(35) Candolfi, C.; Lenoir, B.; Chubilleau, C.; Dauscher, A.; Guilmeau, E. *J. Phys.: Condens. Matter* **2010**, *22*, 025801.
(36) Shi, X.; Pei, Y.; Snyder, G.; Chen, L. *Energy Environ. Sci.* **2011**, *4*, 4086−4095.
(37) Candolfi, C.; Lenoir, B.; Dauscher, A.; Koza, M. M.; De Boissieu, M.; Sternik, M.; Parlinski, K. *Phys. Rev. B: Condens. Matter Mater. Phys.* **2011**, *84*, 224306.
(38) Bukowski, Z.; Badurski, D.; Stepién-Damm, J.; Troc, R. *Solid State Commun.* **2002**, *123*, 283−286.
(39) Candolfi, C.; Lenoir, B.; Dauscher, A.; Bellouard, C.; Hejtmanek, J.; Santava, E.; Tobola, J. *Phys. Rev. Lett.* **2007**, *99*, 155127.
(40) Candolfi, C.; Lenoir, B.; Dauscher, A.; Hejtmanek, J.; Santava, E.; Tobola, J. *Phys. Rev. B: Condens. Matter Mater. Phys.* **2008**, *77*, 092509.
(41) Wiendlocha, B.; Tobola, J.; Sternik, M.; Kaprzyk, S.; Parlinski, K.; Oles, A. M. *Phys. Rev. B: Condens. Matter Mater. Phys.* **2008**, *78*, 060507.
(42) Wiendlocha, B.; Sternik, M. *Intermetallics* **2014**, *53*, 150.
(43) Parker, D.; Du, M.-H.; Singh, D. J. *Phys. Rev. B: Condens. Matter Mater. Phys.* **2011**, *83*, 245111.
(44) Bansal, D.; Li, C. W.; Said, A. H.; Abernathy, D. L.; Yan, J.; Delaire, O. *Phys. Rev. B: Condens. Matter Mater. Phys.* **2015**, *92*, 214301.

DOI: 10.1021/acs.inorgchem.6b00781
Inorg. Chem. XXXX, XXX, XXX−XXX